



HAL
open science

Effects of Mn or Al incorporation on the structure, composition, and As(III) adsorption of oxidized green rust

Xiaoming Wang, Xuewen Li, Lanxin Wang, Bruno Lanson, Mengqiang Zhu, Chaoyun Ying, Xinran Liang, Xionghan Feng

► To cite this version:

Xiaoming Wang, Xuewen Li, Lanxin Wang, Bruno Lanson, Mengqiang Zhu, et al.. Effects of Mn or Al incorporation on the structure, composition, and As(III) adsorption of oxidized green rust. *Chemical Geology*, 2022, 611, pp.121124. 10.1016/j.chemgeo.2022.121124 . insu-03833507

HAL Id: insu-03833507

<https://insu.hal.science/insu-03833507>

Submitted on 28 Oct 2022

HAL is a multi-disciplinary open access archive for the deposit and dissemination of scientific research documents, whether they are published or not. The documents may come from teaching and research institutions in France or abroad, or from public or private research centers.

L'archive ouverte pluridisciplinaire **HAL**, est destinée au dépôt et à la diffusion de documents scientifiques de niveau recherche, publiés ou non, émanant des établissements d'enseignement et de recherche français ou étrangers, des laboratoires publics ou privés.

18 **Abstract**

19 The trace cations could incorporate into the structure of oxidized green rust (Ox-GR), a layered
20 reactive Fe(III) oxyhydroxide formed from rapid oxidation of GR, but the effects of cation
21 incorporation on the mineralogical properties and surface reactivity of Ox-GR remain unknown. Here,
22 we synthesized Mn- or Al-incorporated Ox-GR by oxidation of sulfate-bearing GR and determined
23 their structure, elemental composition and distribution, and As(III) adsorption using macroscopic
24 batch experiments and spectroscopic analyses. The presence of Mn or Al favored sulfate
25 accumulation in Ox-GR, with some sulfate being homogeneously distributed in the interlayer, others
26 adsorption on the mineral edge sites. Majority of Mn and Al entered the layer structure of Ox-GR as
27 Mn(III) and Al(III) through isomorphous substitution, leading to the increased d-spacing of (001)
28 plane but slightly decreased d-spacing of a-b planes. The Al incorporation remarkably reduced the
29 structural ordering degree and Fe octahedral layers of Ox-GR through inhibiting the crystal-growth
30 of GR. Compared with the Mn incorporation, the Al incorporation led to a more pronounced structural
31 variation of Ox-GR, ascribed to its higher isomorphic substitution amount. The incorporation of Mn
32 or Al both promoted As(III) adsorption per mineral mass, predominantly due to the increase of sulfate
33 content and/or specific surface area, and the incorporated Mn(III) could oxidize As(III). As(III)
34 adsorption on Ox-GR involved both surface sulfate and >Fe-OH/OH₂ groups exchange, forming a
35 bidentate-binuclear inner-sphere surface complexation. These new insights into the structure and
36 reactivity of Ox-GR are essential to understanding environmental behavior of GR and its derivative
37 Ox-GR in artificial and environmental settings.

38 **Keywords:** Oxidized green rust; Mn/Al incorporation; structure; composition; elemental distribution;
39 As adsorption

40 **1. Introduction**

41 Green Rust (GR) is a layered double hydroxide (LDH) mineral and composed of positively
42 charged Fe(II)-Fe(III)-hydroxide layers with interlayers hosting anions (*e.g.*, SO_4^{2-}) and H_2O
43 molecules (Ruby et al., 2006). The GR has been identified in various environmental settings such as
44 flooded and paddy soils, groundwater, sediments, etc. (Trolard and Bourrié, 2006; Trolard et al., 1997),
45 and exerts a strong control on the mobility, toxicity, and redox transformation of organic and inorganic
46 pollutants in those environments (Usman et al., 2018). When exposed to air or contacted with oxidants,
47 GR gradually transforms to goethite, magnetite, and lepidocrocite through dissolution-oxidation-
48 precipitation (DOP) and to oxidized green rust (Ox-GR) through solid-state oxidation (SSO) (Feng
49 et al., 2015; Inoue et al., 2007; Legrand et al., 2004; Refait et al., 2007; Wang et al., 2013).

50 Ox-GR exhibits a similar layer structure as GR but only contains Fe(III) (Refait et al., 2003). It
51 can form from direct oxidation of GR suspension by strong oxidants such as H_2O_2 (Legrand et al.,
52 2004; Refait et al., 2003) and air oxidation of GR suspension in the presence of oxyanions (*e.g.*,
53 phosphate, silicate, or arsenate) (Feng et al., 2015; Refait et al., 2007; Wang et al., 2017). The key
54 process of the formation of Ox-GR through GR oxidation is the stabilization of the layer structure by
55 oxyanion adsorption on the edge sites (Feng et al., 2015; Legrand et al., 2004; Wang et al., 2017).
56 The reactive oxygen species (ROS) with strong oxidation ability and oxyanion inhibitors (*e.g.*,
57 phosphate and silicate) are ubiquitous in natural environments (Cruz et al., 2013; Tong et al., 2016),
58 which provides suitable conditions for the formation of Ox-GR through GR oxidation. Previous
59 studies relevant to Ox-GR mainly focused on the synthesis of single-sheet Ox-GR with dodecanoate
60 stabilizing the structure of GR (Ayala-Luis et al., 2010; Huang et al., 2013; Yin et al., 2019a) and its
61 use as adsorbent to efficiently remove arsenate and phosphate from wastewater (Barthelemy et al.,

62 [2012; Yin et al., 2019b](#)). In addition, Ox-GR could serve as an electron acceptor for Fe reducing
63 bacteria and directly transform to GR ([Jorand et al., 2007](#)). However, the structure, composition, and
64 surface reactivity of Ox-GR are still poorly understood.

65 The cations of Al and Mn are abundant in natural environments and can enter the structure of Fe
66 (oxyhydr)oxides through isomorphous substitution, changing their structure and surface activity
67 ([Cornell and Schwertmann, 2003](#)). Naturally occurring GR usually contains trace cations through
68 adsorption and/or co-precipitation ([Genin and Ruby, 2004; Johnson et al., 2014; Johnson et al., 2015](#)).
69 A lot of studies have indicated that the Al(III) ions can replace Fe(III) in the layer of GR during its
70 formation, thereby remarkably decreasing the crystallinity and coherent scattering domain size,
71 varying the cell parameters, and favoring its transformation to goethite ([Dideriksen et al., 2022; Genin
72 and Ruby, 2004; Refait et al., 2017; Ruby et al., 2008; Trolard and Bourri , 2006](#)). In contrast, the
73 effect of Mn on the crystallization of GR depends on its concentration, *i.e.*, low Mn concentration
74 slightly favors its crystallization but high Mn concentration slightly inhibits ([Wang et al., 2019](#)); the
75 presence of Mn promotes the formation of lepidocrocite and magnetite during GR transformation
76 ([Inoue et al., 2007; Wang et al., 2019](#)). Therefore, when the Al- or Mn-bearing GR was rapidly
77 oxidized to Ox-GR, the incorporation of Al or Mn in Ox-GR will undoubtedly change the structure
78 and composition of Ox-GR, which needs to be clarified.

79 Additionally, GR is one of the most effective Fe (oxyhydr)oxides for arsenic (As) sequestration
80 in the anoxic subsurface environments ([Perez et al., 2020; Perez et al., 2019; Perez et al., 2021; Su
81 and Wilkin, 2005](#)), and the As(III) and As(V) uptake by GR are substantially affected by the pH and
82 coexisting ions ([Perez et al., 2019](#)). The transformation of GR in the presence of As(V) can greatly
83 accumulate As(V), leading to the formation of Ox-GR at high As(V) loadings ([Wang et al., 2017](#)).

84 Adsorption of As(V) onto single-sheet Ox-GR is very fast, with 80% of total As(V) adsorbed within
85 10 min, and involves protonated and deprotonated bidentate inner-sphere complexes (Yin et al.,
86 2019b), but the As(III) adsorption behavior on Ox-GR and what are the effects of Mn or Al
87 incorporation remain unknown.

88 The objectives of this study are, therefore, to determine the effects of Mn or Al incorporation on
89 the structure, elemental composition and distribution, and As(III) adsorption behaviors of the Ox-GR.
90 To reach these aims, we firstly synthesized the Mn- and Al-incorporated Ox-GR samples by rapid
91 oxidation of sulfate-bearing GR with the presence of Mn or Al. The structure, composition, elemental
92 speciation and distribution of these Ox-GR samples were then characterized by X-ray diffraction
93 (XRD), Fourier transform infrared (FTIR) spectroscopy, high-resolution transmission electron
94 microscopy (HRTEM) combined with selected area electron diffraction (SAED) and X-ray energy
95 dispersive spectroscopy (EDS), Mn K-edge X-ray absorption near-edge structure (XANES)
96 spectroscopy, and acidic dissolution experiments. Finally, the As(III) adsorption behaviors on the Mn-
97 or Al-incorporated Ox-GR samples were determined by batch adsorption kinetics combined with the
98 release of SO_4^{2-} , Mn^{2+} , and Al^{3+} and partial products analyses with X-ray photoelectron spectroscopy
99 (XPS) and As K-edge X-ray absorption spectroscopy (XAS).

100 **2. Materials and methods**

101 *2.1. Synthesis of Mn- or Al-incorporated Ox-GR*

102 The GR was synthesized by air oxidation of Fe^{2+} in the presence of sulfate and Mn^{2+} or Al^{3+} , with
103 varying initial Fe/Mn molar ratios of 1, 6, and 24 and Fe/Al molar ratios of 6 and 36. A system with
104 addition of Na_2SO_4 solution (Fe/Na molar ratio of 24) was used as control. Specifically, 10 mL MeSO_4
105 (Me = Mn, Al, or Na) with different concentrations was mixed with 90 mL of 0.211 mM NaOH and

106 90 mL of 0.127 mM FeSO₄ (OH/Fe = 1.66) in a 300 mL reaction cell. The mixed solution was
107 oxidized in the open air under stirring at 25 °C. The suspension pH and redox potential (Eh) were
108 monitored respectively with a pH electrode (Metrohm 6.0280.300) and a Pt electrode (Metrohm
109 6.0451.100), both of which referred to an Ag/AgCl reference electrode. The GR formed completely
110 when the suspension pH and Eh curves reached the first inflection points (Christiansen et al., 2009)
111 (arrow A in Fig. S1). Two mL of suspension was sampled at that time point and filtered through a
112 0.22 μm membrane for XRD analysis.

113 After the GR formed completely, 10 mL of 0.8 M HEPES was added to buffer the suspension pH
114 (arrow B in Fig. S1), avoiding a sharp drop of suspension pH caused by the abundant H⁺ release
115 during GR oxidation. After stirring for ~3 min, 2.5 mL of 30% H₂O₂ was added to oxidize the GR
116 (arrow C in Fig. S1). The oxidation reaction lasted for 40 min, during which 2 mL suspension were
117 sampled at different time intervals and filtered through 0.22 μm membrane for XRD analysis. The
118 specific variations of suspension pH and Eh during the formation of Ox-GR were described in the
119 Electronic Supplementary Material (SM-1). The final Mn- or Al-incorporated Ox-GR suspension was
120 centrifuged, washed, freeze dried, ground, and stored in a desiccator for subsequent characterizations.

121 2.2. Characterizations of Ox-GR

122 2.2.1. Acidic dissolution experiments

123 To obtain the chemical composition of Ox-GR samples, 10 mg dry sample was dissolved in 10
124 mL of 4 M HCl at 25°C for 2 h. Additionally, acidic dissolution kinetics of two selected Ox-GR dried
125 samples (*i.e.*, initial Fe/Mn = 24 and Fe/Al = 36) were examined to determine the dissolution rate and
126 spatial distribution of Mn, Al, and SO₄²⁻ in the minerals. Briefly, 48 mg sample was dissolved in 150
127 mL of 2 M HCl for 2 h at 25°C under stirring condition. At pre-set time intervals, 2.5 mL suspension

128 was sampled and filtered through a 0.22 μm membrane filter. The concentrations of dissolved Fe, S,
129 Mn, and Al in the filtrates were determined by inductively coupled plasma optical emission
130 spectroscopy (ICP-OES).

131 2.2.2. XRD, FTIR, specific surface area, and Zeta potential

132 The XRD patterns of Ox-GR samples were measured with a Bruker D8 ADVANCE X-ray
133 diffractometer (Cu $K\alpha$, $\lambda = 0.15418$ nm) with a scanning rate of 10 $^\circ/\text{min}$ for the intermediate wet
134 samples and 1 $^\circ/\text{min}$ for the final dry samples at a step size of 0.02 $^\circ$. The wet samples were coated
135 with a thin layer of glycerol to minimize oxidation during data collection (Hansen et al., 1994). The
136 FTIR spectra of the dry samples, mixed with dry KBr (~1% sample weight), were measured over the
137 wavenumber range of 4000 - 400 cm^{-1} with a resolution of 4 cm^{-1} and 64 scans against the air
138 background (Bruker VERTEX 70). The specific surface area (SSA) of Ox-GR samples, determined
139 by the five-point BET method, was measured using N_2 adsorption at 77 K (ASAP 2460, micromeritics)
140 after vacuum degassing at 80 $^\circ\text{C}$ for 3 h. The Zeta potential of 2 g/L Ox-GR suspension, equilibrated
141 at different pHs (pH 4 - 9) for 8 h in 0.05 M NaNO_3 solution, was measured using a Malvern Zetasizer
142 ZEN 3600.

143 2.2.3. HRTEM-SAED-EDS and Mn K-edge XANES spectroscopic analyses

144 HRTEM images and SAED patterns of the Ox-GR samples were collected using a Talos F200S
145 TEM. X-ray EDS were recorded using an Oxford IE250 system. Mn K-edge XANES spectra were
146 collected in fluorescence mode at beamline 1W2B of Beijing Synchrotron Radiation Facility (BSRF)
147 using a Si(111) double crystal monochromator. Multiple scans (≥ 2) were conducted for each sample
148 and the averaged spectra were used. All data were processed using software Athena (Ravel and
149 Newville, 2005). The atomic fractions of Mn(II), Mn(III), and Mn(IV) in the Mn-incorporated Ox-

150 GR were determined using the Combo method developed by Manceau et al. (2012), with an
151 uncertainty of the Mn average valence being ~ 0.04 . The spectra of Mn(II), Mn(III), and Mn(IV)
152 reference compounds used for linear combination fitting (LCF) analysis were given in Fig S2.

153 2.3. As(III) adsorption kinetics on the Ox-GR samples

154 As(III) adsorption kinetics were investigated by reacting 2 g/L Ox-GR with 1 mM As(III) at pH
155 5 ± 0.05 and 25°C in 0.05 M NaNO₃ solution. The conditions were relevant to the weak acidic soil
156 environments. The total suspension volume was 100 mL and the reaction lasted for 8 h under stirring
157 condition. The mineral suspension (96.67 mL) was equilibrated at pH 5 and 0.05 M NaNO₃ for 10 h
158 before addition of 3.33 mL of 30 mM As(III) solution. At regular time intervals, a 2 mL suspension
159 was sampled and immediately filtered through a 0.22 μm membrane filter. The adsorption kinetics
160 were conducted in duplicate. The concentrations of dissolved As, SO₄²⁻, Mn, and Al were measured
161 by ICP-OES. The amount of As adsorbed was calculated as the difference between the initial and
162 remaining As in the solution. To determine whether As(III) was oxidized to As(V), 1 mL suspension
163 after reaction for 8 h was mixed with 4 mL of 1 M NaOH in 10 mL tubes and shaken for 1 h. The
164 dissolved As(V) after desorption was determined by the molybdate blue colorimetric method using a
165 UV-vis spectrophotometer.

166 A pseudo-second-order kinetic equation was used to model the As adsorption kinetics:

$$167 \quad \frac{dq_t}{dt} = k_2 (q_e - q_t)^2 \quad (1)$$

168 Where the q_e and q_t are, respectively, the amount of As adsorbed ($\mu\text{mol/g}$) at equilibrium and an
169 given time of t ; k is the rate constant $\text{g}/\mu\text{mol}/\text{min}$. The linear equation of the pseudo-second-order
170 kinetics can be obtained by integrating the above equation with the boundary conditions of $t = 0, q_t =$
171 0 and $t = t, q_t = q_e$:

172
$$\frac{t}{q_t} = \frac{1}{k_2 q_e^2} + \frac{t}{q_e} \quad (2)$$

173 The dry Ox-GR samples with Fe/Mn = 26 before and after As(III) adsorption were analyzed by
174 XPS (VG Multilab2000) with an Al K α X-ray source (1486 eV). The narrow spectral changes of Mn_{2p}
175 and O_{1s} were scanned at a pass energy of 25 eV and an energy step size of 0.1 eV. Spectra were
176 charge-corrected to C_{1s} with a binding energy of 284.80 eV collected from the surface adventitious
177 carbon and analyzed with Advantage software. The As K-edge XAS of selected Ox-GR samples after
178 As adsorption were collected in fluorescence mode at beamline 1W2B of BSRF. The data processing
179 and analyses were given in the Supplementary Material (SM-2).

180 **3. Results and discussion**

181 *3.1. Formation of Ox-GR in the presence of Mn or Al*

182 The XRD patterns showed the characteristic peaks of GR(SO₄²⁻) at d-spacing values of ~10.5 Å,
183 ~5.4 Å, and ~3.6 Å (i.e., black lines in Fig. 1a-1c) (Dideriksen et al., 2022; Perez et al., 2019),
184 indicating the formation of GR at all conditions. Compared with the peak intensities of control system
185 (Fig. 1a), the presence of Al³⁺ remarkably inhibited the crystallization of GR (Fig. 1c), consistent with
186 the previous studies (Dideriksen et al., 2022; Refait et al., 2017; Ruby et al., 2008). After the addition
187 of H₂O₂, the GR was quickly oxidized to Ox-GR, resulting in the rapid decrease of suspension pH
188 and increase of suspension Eh (Fig. S1). The d-spacing of basal (001) plane of Ox-GR was slightly
189 smaller than that of GR for the blank system (10.47 Å → 10.33 Å, Fig. 1a), but slightly larger than
190 that of GR with the presence of Mn²⁺ (10.76 Å → 11.15 Å, Fig. 1b) or Al³⁺ (10.62 Å → 10.76 Å, Fig.
191 1c). The d-spacing of (001) plane of layered minerals (e.g., GR, Ox-GR, LDH, and phyllosilicates)
192 includes both layer thickness and interlayer distance (Bergaya and Lagaly, 2013), so the above
193 variations might be caused by the following two reasons. One is that the suspension pH substantially

194 decreases during the oxidation of GR to Ox-GR (Fig. S1), leading to more sulfate adsorption on the
195 surfaces and/or enter into the interlayer (Wang et al., 2018), probably enlarging the interlayer distance;
196 the other is that when Fe^{2+} and Mn^{2+} are oxidized to Fe(III) and Mn(III/IV) after GR oxidation, the
197 Fe or Mn with a higher valence has a lower ionic radius compared to their divalent counterparts
198 (Sposito, 2016) (Table S1), leading to the shrink of MeO_6 octahedra and thus decreasing the layer
199 thickness. Noted that the slight shifts in the position of the (001) plane may be caused by the
200 instrument error, which cannot be totally excluded due to the poorly crystalized property of GR,
201 although our instrument was calibrated by corundum reference prior to the XRD measurements.

202 Compared with the diffraction peak intensities of GR for the blank and $\text{Fe}/\text{Mn} = 24$, the (001)
203 plane of Ox-GR weakened and (002) and (003) planes of Ox-GR even disappeared (Fig. 1a and 1b),
204 suggesting the loss of periodicity to some extent along the c^* -axis during GR oxidation. Additionally,
205 the d-spacing of (001) plane of Ox-GR substantially decreased after sample drying (Fig. 1d-1f),
206 similar to the formation of birnessite from buserite with drying (Feng et al., 2005), confirming the
207 presence of water molecules in the interlayer. These water molecules probably form sulfate
208 outer-sphere complexes with sulfate through hydrogen (H)-bonding (Wang et al., 2015), in addition
209 to sulfate inner-sphere complexes, to stabilize the layer structure. Furthermore, the peak intensity of
210 (001) plane (*i.e.*, c^* -axis direction) decreased while those of a-b planes (*i.e.*, peaks at $\sim 2.55 \text{ \AA}$ and
211 $\sim 1.48 \text{ \AA}$) increased with drying (Fig. 1d-1f), probably ascribed to the change of preferred orientation
212 and the slight structural rearrangement during sample washing and drying.

213 3.2. Chemical composition, SSA, and Zeta potential of Ox-GR samples

214 The chemical compositions of the dry Ox-GR samples showed that the Fe/Me ratios in the final
215 products were higher than the initial values, especially for the Mn system (Table 1), indicating that a

216 certain amount of Mn/Al ions remained in the solution during the formation of Ox-GR, caused by the
217 decrease of suspension pH (Fig. S1) that lead to the release of Mn/Al from minerals. Thus, the Fe/Me
218 ratios in the final products were used to describe the samples, rather than the initial Fe/Me ratios.
219 With increasing Mn or Al content in Ox-GR, the Me/S (Me = Fe + Mn/Al) molar ratios gradually
220 decreased (Table1), suggesting that the presence of Mn or Al lead to more sulfate accumulated in the
221 mineral, including surface adsorption and interlayer incorporation. Compared with the Mn system at
222 the similar loading (*i.e.*, Fe/Me = 40), more sulfate were accumulated for the Al system (Table1),
223 ascribed to the stronger interaction between sulfate and Al³⁺ (Sposito, 2016). The SSA of Ox-GR
224 slightly increased from 61 m²/g for Fe/Na = 24 to 68 m²/g for Fe/Mn = 19 with increasing Mn content,
225 while it firstly increased to 113 m²/g for Fe/Al = 40 and then remarkably decreased to 37 m²/g for
226 Fe/Al = 6.3 with increasing Al content (Table1). The variation of SSA should be related to the different
227 particle size, crystallinity, elemental composition and content, and particle aggregation of Ox-GR
228 samples (Cornell and Schwertmann, 2003). The PZC of Ox-GR changed between 6.8 and 7.4, closing
229 to the PZC value of single-sheet Ox-GR (*i.e.*, pH 7.8) (Yin et al., 2019b), and the presence of Mn or
230 Al slightly enhanced its PZC, with the Mn system more obvious (Fig. S3).

231 3.3. Structure and morphology of Ox-GR samples

232 The XRD patterns of dry Ox-GR samples showed that the peak intensity and the full-width at
233 half-maximum of Mn-bearing Ox-GR slightly increased compared to the blank Ox-GR (*i.e.*, Fe/Na =
234 24), but changed subtly with increasing Mn content (Fig. 2a-2d). In contrast, the crystallinity of
235 Ox-GR decreased substantially with the presence of Al (Fig. 2a-2d). The diffraction peaks of Ox-GR
236 with Fe/Al = 6.3 almost disappeared (Fig. 2a-2d), suggesting that the presence of Al remarkably
237 enhanced the degree of structural disorder, leading to the stacking of only few Fe octahedral layers

238 along the c^* -axis. This should be ascribed to that the presence of Al substantially inhibits the
239 crystal-growth of GR precursor (Fig. 1c) (Dideriksen et al., 2022; Refait et al., 2017), thus resulting
240 in the poor crystalized of Ox-GR. In addition, with the increase of Mn or Al content, the d-spacing of
241 (001) plane along the c-axis direction gradually shifted to a higher value (*i.e.*, lower 2θ angle) (Fig.
242 2a and 2b), which might involve the following two reasons. On one aspect, the incorporation of Mn
243 or Al enhances the sulfate content (Table 1), probably resulting in the increase of interlayer sulfate
244 density and thus enlarging the interlayer distance. On the other aspect, the electronegativity of Mn
245 (1.55) and Al (1.61) is lower than that of Fe (1.83) (Sposito, 2016) (Table S1), so the electronegativity
246 in each layer decreases after Mn or Al incorporation, resulting in weaker H-bonding between
247 interlayer sulfate and layer Me-OH sites (*i.e.*, sulfate outer-sphere complex) (Liao et al., 2020), thus
248 leading to an increase of interlayer distance.

249 On the contrary, with the increase of Mn or Al content, the d-spacing values of a-b plane shifted
250 to a lower value (*i.e.*, higher 2θ angle) (Fig. 2c and 2d), most likely ascribed to the isomorphic
251 substitution of Fe by Mn and Al. The ionic radii of Al(III) (0.54 Å) is lower than that of Fe(III) (0.65
252 Å), leading to the lattice contract and thus the decrease of unit-cell parameters and d-spacing, similar
253 to that of Al-incorporated lepidocrocite (Liao et al., 2020). As to the Mn system, although Mn(III)
254 and Fe(III) cations have similar ionic radii and charge (Table S1), the Mn(III) substitution may induce
255 a decrease of in-plane unit-cell parameters owing to the Jahn-Teller distortion of Mn(III) octahedral
256 (Alvarez et al., 2006), thus decreasing the d-spacing. Compared with the d-spacing values of Mn
257 system, those of Al system showed more remarkably variation (Fig. 2a-2d), due to the higher
258 isomorphic substitution of Fe by Al (Table 1). Therefore, the incorporation of Mn or Al substantially
259 modified the crystal structure of Ox-GR, with the Al system more obvious.

260 The SAED images of Ox-GR samples exhibited two polycrystalline rings (Fig. 3b-3f),
261 corresponding to the two reflections of a-b plane (Fig. 2a). The calculated d-spacing values of a-b
262 plane from the ED rings slightly decreased with the presence of Mn or Al (Fig. 3b-3e), consistent
263 with the results of XRD patterns (Fig. 2a) and the lattice spacing analyses from the HRTEM images
264 (Fig. S4a-S4d). In addition, the HRTEM images along the layer stacking direction showed that the d-
265 spacing values of (001) plane are ~ 8.45 Å for Fe/Na = 24 (Fig. 3g) and ~ 8.75 Å for Fe/Mn = 19 (Fig.
266 3h), meaning that the presence of Mn increased the d-spacing of (001) plane, in agreement with the
267 XRD results (Fig. 2a-2d). The small difference of the d-spacing values between XRD and TEM
268 analyses probably comes from the calculation deviation due to the poor crystallinity of this mineral.

269 The FTIR spectra of the Ox-GR samples showed the characteristic Fe-O band at 696 cm^{-1} (Fig.
270 2e and 2f), which slightly shifted to a higher wavenumber with the presence of Mn or Al, especially
271 for the Al system, probably due to the structural incorporation. The sulfate in Ox-GR exhibited
272 asymmetric $\nu_3(\text{SO}_4)$ vibration bands at 1060 cm^{-1} , 1121 cm^{-1} and 1185 cm^{-1} , $\nu_1(\text{SO}_4)$ band at 978 cm^{-1} ,
273 and $\nu_4(\text{SO}_4)$ band at 619 cm^{-1} (Fig. 2e and 2f), similar to the features of sulfate adsorption on
274 hematite (Wang et al., 2018) and structural sulfate in schwertmannite (Wang et al., 2015). In addition,
275 the $\nu_1(\text{SO}_4)$ band shifted to a higher wavenumber, while the $\nu_4(\text{SO}_4)$ band shifted to a lower
276 wavenumber with increasing Mn or Al content (Fig. 2e and 2f), probably owing to partial SO_4
277 adsorption onto Mn-OH or Al-OH sites and/or the formation of Mn/Al- SO_4 ternary complexes on
278 mineral edge surface (Johnston and Chrysochoou, 2016; Swedlund et al., 2009).

279 Besides the structure and composition variations, the presence of Mn or Al in Ox-GR also
280 affected the particle morphology and size. The GR and Ox-GR crystals were approximately
281 hexagonal flakes (Fig. 3a-3f). The particle surface of GR was smooth (Fig. 3a), while that of the Ox-

282 GR showed some small cracks (Fig. 3b-3d). This might be due to that the in-situ oxidation of Fe²⁺ to
283 Fe³⁺ decreases the ionic radius of Fe (*i.e.*, 0.078 nm for Fe²⁺ versus 0.065 nm for Fe³⁺, Table S1),
284 resulting in the lattice contraction and the increased degree of structural disorder at the c*-axis
285 direction (Fig. 1a-1c). Compared to the blank sample, the presence of Mn or Al in Ox-GR reduced
286 the particle size, with the Al system more obvious (Fig. 3b-3f), consistent with the XRD analyses
287 (Fig. 2a). The Ox-GR particles for the Al system exhibited obvious aggregation features due to the
288 small particle size (Fig. 3f). Therefore, the SSA increase of Ox-GR with Fe/Al = 40 should be due to
289 the decrease of particle size and crystallinity, while the substantial decrease of SSA for the Ox-GR
290 with Fe/Al = 6.3 is probably caused by the presence of abundant SO₄²⁻ (Table1) and remarkable
291 particle aggregation (Fig. 3f) that could not be penetrated by N₂.

292 3.4. Speciation and distribution of Mn, Al, and sulfate in Ox-GR samples

293 The quantitative analyses of Mn K-edge XANES spectra showed that Mn mainly existed in the
294 form of Mn(III) (~80%) in the Mn-bearing Ox-GR, with minor Mn(II) and little Mn(IV) (Fig. 4),
295 indicating that most Mn(II) were oxidized to Mn(III) during the oxidation of GR to Ox-GR. The initial
296 Mn concentration seemed no obvious effects on the proportion of different Mn valence in the final
297 products (Fig. 4b).

298 The acidic dissolution kinetics of the products can reflect the elemental spatial distribution in the
299 Ox-GR (Cornell and Schwertmann, 2003). The selected two Ox-GR samples (*i.e.*, Fe/Mn = 40 and
300 Fe/Al = 40) were generally dissolved completely within 30 min, and the release kinetics of Fe, Mn,
301 Al, and S from the mineral displayed a similar trend to each other (Fig. 5a and 5b). In addition, the
302 release ratios of Mn, Al, and SO₄²⁻ all exhibited a positive linear correlation with that of Fe during the
303 dissolution kinetics (Fig. 5c and 5d), indicating that Mn, Al, and S were largely uniformly distributed

304 in the mineral structure, in addition to the surface adsorption. Consistently, the X-ray EDS mappings
305 of Ox-GR samples showed that the elemental distribution of Fe, S, O, Mn, and Al basically coincided
306 with the particle size and thickness, with thicker areas showing higher elemental contents (Fig. S5),
307 further suggesting the homogenous distribution of these elements in the mineral.

308 The intercept of the fitted lines can roughly reflect the proportion of the ion adsorbed on mineral
309 surfaces, with a larger intercept representing a higher proportion of adsorption (Cornell and
310 Schwertmann, 2003). Accordingly, the fractions of sulfate and Mn located on mineral surface were,
311 respectively, 0.22 and 0.1 for Fe/Mn = 40, while those of sulfate and Al were, respectively, 0.45 and
312 0.16 for Fe/Al = 40 (Fig. 5c and 5d). It means that Al incorporation led to a higher proportion of
313 sulfate adsorption on the mineral surface than Mn incorporation at the similar Al/Mn loading.
314 Considering that the intercepts of Mn and Al were relatively small (*i.e.*, 0.10 and 0.16) (Fig. 5c and
315 5d), majority of Mn and Al were distributed in the octahedral layers of the mineral.

316 3.5. Structural incorporation of Mn or Al into the Ox-GR

317 According to the analyses of XRD patterns (Fig. 2a-2d), FTIR spectra (Fig. 2e and 2f), X-ray
318 EDS mapping (Fig. S5), and acid dissolution kinetics (Fig. 5), we can conclude that majority of Mn
319 and Al were structurally incorporated into the layers of Ox-GR through isomorphous substitution,
320 while SO_4^{2-} were distributed both on the mineral surface and in the interlayers of Ox-GR (Fig. 2e, 2f,
321 and 5). The surface SO_4^{2-} likely formed binary and/or SO_4^{2-} - Mn^{2+} / Al^{3+} ternary complexes (Swedlund
322 et al., 2009). The increased sulfate content in Ox-GR with Mn or Al incorporation (Table 1) might be
323 related to the electrostatic attraction and/or the formation of SO_4^{2-} - Mn^{2+} / Al^{3+} ternary complexes on
324 the mineral surface (probably minor in the interlayer). Compared with the Mn system, more sulfate
325 adsorbed on the mineral surface for the Al system (Fig. 5), due to the stronger interaction between

326 Al³⁺ and sulfate (Sposito, 2016). The Mn species that entered in the structure of Ox-GR was most
327 likely Mn(III), probably with minor Mn(IV) (Fig. 4), due to the similar charge and ionic radius of
328 Mn(III) and Fe(III) (Table S1), consistent with that of Mn incorporated into other Fe (oxyhydr)oxides
329 (Cornell and Schwertmann, 2003).

330 3.6. As(III) adsorption-oxidation on Ox-GR samples

331 The As(III) adsorption kinetics on Ox-GR exhibited that arsenic adsorption increased rapidly in
332 the initial stage, and then gradually reach an adsorption equilibrium within 8 h (Fig. 6a). To obtain
333 the amount of As adsorbed at the equilibrium (q_e) and adsorption rate constant (k_2), the As adsorption
334 kinetics were modeled by a pseudo-second-order equation as a previous study (Yin et al., 2019b), and
335 the fitted results were summarized in Fig. 6b and Table S2. The high goodness of the fits ($R^2 > 0.95$)
336 indicated that the As adsorption kinetics on Ox-GR can be described by the pseudo-second-order
337 kinetic model (Table S2). Ascribed to the particle aggregation of Ox-GR (Fig. 3), their SSA will be
338 underestimated through the measurement of N₂-BET method (Villalobos and Antelo, 2011), so we
339 only compared the As(III) adsorption per mineral mass. Compared with the q_e of FeNa = 24 (*i.e.*, 351
340 $\mu\text{mol/g}$), the incorporation of Mn and Al in Ox-GR both promoted the As adsorption. The q_e of Mn-
341 bearing Ox-GR gradually increased from 364 $\mu\text{mol/g}$ for Fe/Mn = 40 to 442 $\mu\text{mol/g}$ for Fe/Mn = 19,
342 while those of Al-incorporated Ox-GR were similar, *i.e.*, 429 $\mu\text{mol/g}$ for Fe/Al = 40 and 429 $\mu\text{mol/g}$
343 for Fe/Al = 6.3 (Table S2). Additionally, the obtained k_2 values of Ox-GR samples ranged from
344 3.90×10^{-4} to 5.02×10^{-4} $\text{g}/\mu\text{mol}/\text{min}$; the k_2 of Fe/Al = 40 was the highest while that of Fe/Al = 6.3 was
345 the lowest (Table S2), probably depended on their SSA (Table 1). These fitted parameters of q_e and
346 k_2 were comparable with those of As(V) adsorption on single-sheet Ox-GR (Yin et al., 2019b).

347 After As(III) adsorption by Ox-GR samples for 8 h, minor As(III) were oxidized to As(V),

348 especially for the Mn system. The ratio of As(V)/total As in the suspension (including solution and
349 solid) increased from 1.4% for Fe/Na = 24 to 22.4% for Fe/Mn = 19 and to 2.5% for Fe/Al = 6.3 (Fig.
350 6e), suggesting that the presence of Mn in Ox-GR remarkably promoted As(III) oxidation, while no
351 promotion effects occurred for Al system. Although minor As(III) were oxidized to As(V) in the
352 presence of Mn (Fig. 6e), As(III) was the main As species adsorbed on mineral surfaces (Fig. S6).
353 The As K-edge EXAFS spectra of the Mn-incorporated Ox-GR samples after As(III) adsorption were
354 shown in Fig. 7 and the fitted parameters were summarized in Table S3. The similar spectral features
355 suggested little variation in the local coordination environment of As in the presence of Mn, despite
356 partial oxidation. The dominant oscillatory pattern in the k space corresponded to the As-O peak in
357 Fourier transform, fitted with CN_{As-O} of 2.9 – 3.1 and an As-O bond length of 1.77 Å. The second
358 peak mainly resulted from the multiple-scattering contribution of As-O-O, fitted with an average As-
359 O-O distance of 3.22 Å. The third peak belonged to the As-Fe atomic pair, with the CN_{As-Fe} ranging
360 from 1.2 - 1.4 and an As-Fe interatomic distance of ~ 3.35 Å. This As-Fe interatomic distance was
361 consistent with a bidentate-binuclear (BB) complex based on the geometric considerations (Jonsson
362 and Sherman, 2008; Ona-Nguema et al., 2009; Perez et al., 2020).

363 The SO_4^{2-} release per mineral mass during kinetics gradually increased with increasing SO_4^{2-}
364 content in Ox-GR and reaction time (Fig. 6c), generally consistent with that of As adsorption (Fig.
365 6a), suggesting that As adsorption on Ox-GR involved SO_4^{2-} exchange. The exchanged SO_4^{2-} should
366 mainly come from the mineral surface rather than interlayer, since the preferred adsorption sites of
367 As(III) are at the GR crystal edges (Perez et al., 2020). The O1s XPS fitting of the Ox-GR with Fe/Mn
368 = 6 showed that after As adsorption the proportions of OH^- and H_2O decreased while that of lattice
369 oxygen (O^{2-}) increased (Fig. 8a and 8b), indicating that As adsorption on Ox-GR also involved ligand

370 exchange with surface Fe-OH/OH₂ groups (Perez et al., 2020; Yin et al., 2019b). Therefore, the As
371 adsorption on Ox-GR involved both anionic and ligand exchange.

372 The As adsorption promoted by the Mn or Al incorporation (Fig. 6a) thus can be explained by
373 the following reasons. Firstly, Mn or Al incorporation in Ox-GR increased the SO₄²⁻ content (Table
374 1), part of which can be anionically exchanged by As (Fig. 6c), thus a higher SO₄²⁻ content in Ox-GR
375 brought more exchangeable adsorption sites and thus greater As adsorption. Secondly, the Mn or Al
376 incorporation enhanced the SSA (except for Fe/Al = 6.3) (Table 1), providing more Fe-OH/OH₂ sites
377 for As adsorption. Thirdly, Mn incorporation in Ox-GR promotes the oxidation of As(III) to As(V)
378 (Fig. 6e), which enhanced the As adsorption because the As(V) exhibits a higher adsorption affinity
379 on Fe oxide surface than As(III) at pH 5 (Dixit and Hering, 2003). Finally, the stacking disorder of
380 Ox-GR remarkably increased with Al incorporation (Fig. 2a), allowing for a higher proportion of
381 sulfate bound to basal surface, thus favoring As(III) anionic exchange.

382 Accordingly, minor dissolved Mn and Al occurred during As adsorption (Fig. 6d). The dissolved
383 Mn increased with increasing Mn content in Ox-GR, but it roughly keeps constant with reaction time
384 (Fig. 6d). The dissolved Mn should be derived from desorption of surface adsorbed Mn²⁺ (Fig. 4b
385 and 5c). In addition, the Mn2p XPS fitting of Fe/Mn = 6 indicates that partial Mn(III/VI) were reduced
386 to Mn(II) during As(III) adsorption (Fig. 8c and 8d), which will lead to few Mn(II) release as well. In
387 contrast, the Al is more difficult to release from mineral surface due to the higher adsorption affinity
388 and hydrolysis constant of Al³⁺ (Sposito, 2016). Minor dissolved Al appeared at the beginning and
389 then quickly re-adsorbed for the Ox-GR with Fe/Al = 6.3 (Fig. 6d), probably attributed to the increase
390 of negative charge at the mineral surface after As adsorption that promotes Al³⁺ re-adsorption through
391 electrostatic effects.

392 **4. Conclusions**

393 GR and its derivative Ox-GR are common in the subsurface environment, playing an extremely
394 critical roles in regulating the biogeochemical processes of trace elements through interfacial
395 reactions. The Ox-GR, a type of LDH mineral, is also an excellent adsorbent for removing
396 contaminants from waste and drinking water (Barthelemy et al., 2012; Yin et al., 2019b). Our study
397 systematically revealed the influence of Mn or Al incorporation on the structure, composition,
398 elemental speciation and distribution, and As(III) adsorption of Ox-GR. The increase of sulfate
399 content in Ox-GR with Mn or Al incorporation will decrease the mobility and availability of sulfate
400 in the relevant environments and change the surface reactivity. The variations of crystal structure of
401 Ox-GR with Mn or Al incorporation give us inspiration for understanding the structure of other LDH
402 minerals with cation isomorphous substitution. Al incorporation substantially reduces the Fe
403 octahedral layers of Ox-GR, leading to the formation of resemble “single-sheet” Ox-GR. The Mn or
404 Al incorporation remarkably changes the structure, composition, and morphology of Ox-GR,
405 promoting the As(III) adsorption of Ox-GR. The As adsorption mechanism involved a BB inner-
406 sphere complex by exchanging both Fe–OH/OH₂ and sulfate groups, which is critical to constructing
407 physically meaningful models. These new insights are essential to understanding the mineralogical
408 properties and surface reactivity of naturally occurring Ox-GR. This study also provides a strategy
409 for synthesis of poorly crystalline Ox-GR (*e.g.*, “single-sheet” mineral) for contaminant removal from
410 wastewater.

411 **Acknowledgments**

412 The authors acknowledge the National Natural Science Foundation of China (No. 42030709 and
413 41977021), the National Key Research and Development Program of China (No. 2020YFC1806803),

414 and the Fundamental Research Funds for the Central Universities (No. 2662019QD015).

415 **Supplementary data**

416 Electronic supplementary information (ESI) available: (1) variation of pH and Eh during the
417 formation of EX-GR, (2) As K-edge XAS spectroscopy collection and analyses, (3) physicochemical
418 properties of elements of Fe, Mn, and Al, (4) Fitting parameters of pseudo second-order kinetic
419 equation and As K-edge EXAFS spectroscopy, (5) Zeta potential, TEM images and EDS mapping of
420 Ox-GR samples, and (6) Mn references spectra.

421 **References**

- 422 Alvarez, M., Rueda, E.H., Sileo, E.E., 2006. Structural characterization and chemical reactivity of
423 synthetic Mn-goethites and hematites. *Chem. Geol.*, 231(4): 288-299.
- 424 Ayala-Luis, K.B., Koch, C.B., Hansen, H.C.B., 2010. Intercalation of linear C9–C16 carboxylates in
425 layered Fe^{II}–Fe^{III}-hydroxides (green rust) via ion exchange. *Appl. Clay Sci.*, 48(3): 334-341.
- 426 Barthelemy, K., Naille, S., Despas, C., Ruby, C., Mallet, M., 2012. Carbonated ferric green rust as a
427 new material for efficient phosphate removal. *J. Colloid Interface Sci.*, 384: 121-127.
- 428 Bergaya, F., Lagaly, G., 2013. *Handbook of Clay Science (2nd, developments in clay science)*.
429 Elsevier.
- 430 Christiansen, B.C., Balic-Zunic, T., Petit, P.O., Frandsen, C., Morup, S., Geckeis, H., Katerinopoulou,
431 A., Stipp, S.L.S., 2009. Composition and structure of an iron-bearing, layered double
432 hydroxide (LDH) - green rust sodium sulphate. *Geochim. Cosmochim. Acta*, 73(12): 3579-
433 3592.
- 434 Cornell, R.M., Schwertmann, U., 2003. *The iron oxides: structure, properties, reactions, occurrences
435 and uses (2nd Edition)*. Wiley-VCH, Weinheim, Germany.
- 436 Cruz, A., Cook, R.L., Dellinger, B., Lomnicki, S.M., Cosgriff, D., 2013. Assessment of
437 environmentally persistent free radicals in soils and sediments from three superfund sites.
438 *Environ. Sci. Proc. Imp.*, 16(1): 44-52.
- 439 Dideriksen, K., Voigt, L., Mangayayam, M.C., Eiby, S.H.J., van Genuchten, C.M., Frandsen, C.,
440 Jensen, K.M.Ø., Stipp, S.L.S., Tobler, D.J., 2022. Order and disorder in layered double
441 hydroxides: lessons learned from the green rust sulfate-nikischerite series. *ACS Earth Space
442 Chem.*, 6(2): 322-332.
- 443 Dixit, S., Hering, J.G., 2003. Comparison of arsenic(V) and arsenic(III) sorption onto iron oxide
444 minerals: implications for arsenic mobility. *Environ. Sci. Technol.*, 37(18): 4182-4189.
- 445 Feng, X., Tan, W., Liu, F., Huang, Q., Liu, X., 2005. Pathways of birnessite formation in alkali
446 medium. *Sci. China Ser. D*, 48(9): 1438-1451.
- 447 Feng, X., Wang, X., Zhu, M., Koopal, L.K., Xu, H., Wang, Y., Liu, F., 2015. Effects of phosphate and
448 silicate on the transformation of hydroxycarbonate green rust to ferric oxyhydroxides.
449 *Geochim. Cosmochim. Acta*, 171: 1-14.

- 450 Genin, J.M.R., Ruby, C., 2004. Anion and cation distributions in Fe(II-III) hydroxysalt green rusts
451 from XRD and Mossbauer analysis (carbonate, chloride, sulphate,...); the "fougerite" mineral.
452 *Solid State Sci.*, 6(7): 705-718.
- 453 Hansen, H.C.B., Borggaard, O.K., Sørensen, J., 1994. Evaluation of the free energy of formation of
454 Fe(II)-Fe(III) hydroxide-sulphate (green rust) and its reduction of nitrite. *Geochim.*
455 *Cosmochim. Acta*, 58(12): 2599-2608.
- 456 Huang, L., Fang, L., Hassenkam, T., Dalby, K.N., Scheckel, K.G., Hansen, H.C.B., 2013. A one-step
457 delamination procedure to form single sheet iron(III)-(oxy)hydroxides. *J. Mater. Chem. A*,
458 1(43): 13664-13671.
- 459 Inoue, K., Kwon, S.K., Kimijima, K., Kanie, K., Muramatsu, A., Shinoda, K., Suzuki, S., Waseda, Y.,
460 2007. Analysis of iron oxyhydroxides and oxides converted from green rust in aqueous
461 solution. *ISIJ Int.*, 47(3): 453-457.
- 462 Johnson, C.A., Freyer, G., Fabisch, M., Caraballo, M.A., Kusel, K., Hochella, M.F., 2014.
463 Observations and assessment of iron oxide and green rust nanoparticles in metal-polluted
464 mine drainage within a steep redox gradient. *Environ. Chem.*, 11(4): 377-391.
- 465 Johnson, C.A., Murayama, M., Kusel, K., Hochella, M.F., 2015. Polycrystallinity of green rust
466 minerals and their synthetic analogs: implications for particle formation and reactivity in
467 complex systems. *Am. Mineral.*, 100(10): 2091-2105.
- 468 Johnston, C.P., Chrysochoou, M., 2016. Mechanisms of chromate, selenate, and sulfate adsorption on
469 Al-substituted ferrihydrite: implications for ferrihydrite surface structure and reactivity.
470 *Environ. Sci. Technol.*, 50(7): 3589-3596.
- 471 Jonsson, J., Sherman, D.M., 2008. Sorption of As(III) and As(V) to siderite, green rust (fougerite)
472 and magnetite: Implications for arsenic release in anoxic groundwaters. *Chem. Geol.*, 255(1-
473 2): 173-181.
- 474 Jorand, F., Zegeye, A., Landry, F., Ruby, C., 2007. Reduction of ferric green rust by *Shewanella*
475 *putrefaciens*. *Lett. Appl. Microbiol.*, 45(5): 515-521.
- 476 Legrand, L., Mazerolles, L., Chaussé, A., 2004. The oxidation of carbonate green rust into ferric
477 phases: solid-state reaction or transformation via solution. *Geochim. Cosmochim. Acta*, 68(17):
478 3497-3507.
- 479 Liao, S., Wang, X., Yin, H., Post, J.F., Feng, X., 2020. Effects of Al substitution on local structure and
480 morphology of lepidocrocite and its phosphate adsorption kinetics. *Geochim. Cosmochim.*
481 *Acta*, 276: 109-121.
- 482 Manceau, A., Marcus, M.A., Grangeon, S., 2012. Determination of Mn valence states in mixed-valent
483 manganates by XANES spectroscopy. *Am. Mineral.*, 97(5-6): 816-827.
- 484 Ona-Nguema, G., Morin, G., Wang, Y.H., Menguy, N., Juillot, F., Olivi, L., Aquilanti, G., Abdelmoula,
485 M., Ruby, C., Bargar, J.R., Guyot, F., Calas, G., Brown, G.E., 2009. Arsenite sequestration at
486 the surface of nano-Fe(OH)₂, ferrous-carbonate hydroxide, and green-rust after bioreduction
487 of arsenic-sorbed lepidocrocite by *Shewanella putrefaciens*. *Geochim. Cosmochim. Acta*,
488 73(5): 1359-1381.
- 489 Perez, J.P.H., Freeman, H.M., Brown, A.P., van Genuchten, C.M., Dideriksen, K., Sari, M., Tobler,
490 D.J., Benning, L.G., 2020. Direct visualization of arsenic binding on green rust sulfate.
491 *Environ. Sci. Technol.*, 54(6): 3297-3305.
- 492 Perez, J.P.H., Freeman, H.M., Schuessler, J.A., Benning, L.G., 2019. The interfacial reactivity of
493 arsenic species with green rust sulfate (GRSO₄). *Sci. Total. Environ.*, 648: 1161-1170.

- 494 Perez, J.P.H., Tobler, D.J., Freeman, H.M., Brown, A.P., Hondow, N.S., van Genuchten, C.M.,
495 Benning, L.G., 2021. Arsenic species delay structural ordering during green rust sulfate
496 crystallization from ferrihydrite. *Environ. Sci. Nano*.
- 497 Ravel, B., Newville, M., 2005. ATHENA, ARTEMIS, HEPHAESTUS: data analysis for X-ray
498 absorption spectroscopy using IFEFFIT. *J. Synchrotron Radiat.*, 12: 537-541.
- 499 Refait, P., Benali, O., Abdelmoula, M., Genin, J.M.R., 2003. Formation of ferric green rust and/or
500 ferrihydrite by fast oxidation of iron(II-III) hydroxychloride green rust. *Corros. Sci.*, 45(11):
501 2435-2449.
- 502 Refait, P., Reffass, M., Landoulsi, J., Sabot, R., Jeannin, M., 2007. Role of phosphate species during
503 the formation and transformation of the Fe(II-III) hydroxycarbonate green rust. *Colloids Surf.*
504 *A Physicochem. Eng. Asp.*, 299(1-3): 29-37.
- 505 Refait, P., Sabot, R., Jeannin, M., 2017. Role of Al(III) and Cr(III) on the formation and oxidation of
506 the Fe(II-III) hydroxysulfate green rust. *Colloids Surf. A Physicochem. Eng. Asp.*, 531: 203-
507 212.
- 508 Ruby, C., Aïssa, R., Géhin, A., Cortot, J., Abdelmoula, M., Génin, J., 2006. Green rusts synthesis by
509 coprecipitation of Fe^{II}-Fe^{III} ions and mass-balance diagram. *C. R. Geosci.*, 338(6-7): 420-432.
- 510 Ruby, C., Abdelmoula, M., Aïssa, R., Medjahdi, G., Brunelli, M., Francois, M., 2008. Aluminium
511 substitution in iron(II-III)-layered double hydroxides: Formation and cationic order. *J. Solid*
512 *State Chem.*, 181(9): 2285-2291.
- 513 Sposito, G., 2016. *The Chemistry of Soil* (3rd Edition). Oxford University Press, New York, NY.
- 514 Su, C., Wilkin, R.T., 2005. Arsenate and arsenite sorption on and arsenite oxidation by iron(II, III)
515 hydroxycarbonate green rust. In: ODay, P. (Ed.), *Advances in Arsenic Research*. American
516 Chemical Society, Washington, DC.
- 517 Swedlund, P.J., Webster, J.G., Miskelly, G.M., 2009. Goethite adsorption of Cu(II), Pb(II), Cd(II),
518 and Zn(II) in the presence of sulfate: Properties of the ternary complex. *Geochim. Cosmochim.*
519 *Acta*, 73(6): 1548-1562.
- 520 Tong, M., Yuan, S., Ma, S., Jin, M., Liu, D., Cheng, D., Liu, X., Gan, Y., Wang, Y., 2016. Production
521 of abundant hydroxyl radicals from oxygenation of subsurface sediments. *Environ. Sci.*
522 *Technol.*, 50(1): 214-21.
- 523 Trolard, F., Bourrié, G., 2006. Structure of fougérite and green rusts and a thermodynamic model for
524 their stabilities. *J. Geochem. Explor.*, 88(1-3): 249-251.
- 525 Trolard, F., Génin, J.M.R., Abdelmoula, M., Bourrie, G., Herbillon, A., 1997. Identification of a green
526 rust mineral in a reductomorphic soil by Mossbauer and Raman spectroscopies. *Geochim.*
527 *Cosmochim. Acta*, 61(5): 1107-1111.
- 528 Usman, M., Byrne, J.M., Chaudhary, A., Orsetti, S., Hanna, K., Ruby, C., Kappler, A., Haderlein,
529 S.B., 2018. Magnetite and green rust: synthesis, properties, and environmental applications of
530 mixed-valent iron minerals. *Chem. Rev.*, 118(7): 3251-3304.
- 531 Villalobos, M., Antelo, J., 2011. A Unified Surface Structural Model for Ferrihydrite: Proton Charge,
532 Electrolyte Binding, and Arsenate Adsorption. *Revista Internacional De Contaminacion*
533 *Ambiental*, 27(2): 139-151.
- 534 Wang, X., Gu, C., Feng, X., Zhu, M., 2015. Sulfate local coordination environment in schwertmannite.
535 *Environ. Sci. Technol.*, 49(17): 10440-10448.
- 536 Wang, X., Liu, F., Tan, W., Feng, X., Koopal, L.K., 2013. Transformation of hydroxycarbonate green
537 rust into crystalline iron (hydr)oxides: influences of reaction conditions and underlying

538 mechanisms. *Chem. Geol.*, 351: 57-65.

539 Wang, X., Peng, J., Liang, X., Zhu, M., Lanson, B., Wang, L., Liang, X., Liu, F., Tan, W., Feng, X.,
540 2019. Effects of Mn^{2+} , Ni^{2+} and Cu^{2+} on the formation and transformation of hydrosulfate
541 green rust: reaction processes and underlying mechanisms. *ACS Earth Space Chem.*, 3: 519-
542 530.

543 Wang, X., Peng, J., Xu, H., Tan, W., Liu, F., Huang, Q., Feng, X., 2017. Influences and mechanisms
544 of As(V) concentration and environmental factors on hydrosulfate green rust transformation.
545 *Acta Chim. Sinica*, 75(6): 608-616.

546 Wang, X., Wang, Z., Peak, D., Tang, Y., Feng, X., Zhu, M., 2018. Quantification of coexisting inner-
547 and outer-sphere complexation of sulfate on hematite surfaces. *ACS Earth Space Chem.*, 2(4):
548 387-398.

549 Yin, Z., Dideriksen, K., Abdelmoula, M., Ruby, C., Michel, F.M., Bjerrum, M.J., Hansen, H.C.B.,
550 2019a. Structure of single sheet iron oxides produced from surfactant interlayered green rusts.
551 *Appl. Clay Sci.*, 170: 86-96.

552 Yin, Z., Lutzenkirchen, J., Finck, N., Celaries, N., Dardenne, K., Hansen, H.C.B., 2019b. Adsorption
553 of arsenic(V) onto single sheet iron oxide: X-ray absorption fine structure and surface
554 complexation. *J. Colloid Interface Sci.*, 554: 433-443.

555

Table 1. Chemical composition and SSA of the dry Mn- or Al-incorporated Ox-GR samples.

Initial Fe/Me ratios	Final Fe/Me ratios	Fe	S	Mn	Al	Molar ratios of (Fe + Mn/Al)/S	SSA (m ² /g)
		(mmol/g)					
Fe/Na = 24	/	10.1	1.25	/	/	8.1	61
Fe/Mn = 24	40	9.0	1.16	0.23	/	8.0	62
Fe/Mn = 6	26	9.2	1.31	0.35	/	7.3	68
Fe/Mn = 1	19	8.9	1.41	0.47	/	6.6	68
Fe/Al = 36	40	8.8	1.40	/	0.22	6.4	113
Fe/Al = 6	6.3	7.2	1.79	/	1.14	4.7	37

558 **Figure captions**

559 **Fig. 1.** XRD patterns of GR (black line) and its oxidation product of Ox-GR (red line) after adding
560 H₂O₂ for ~40 min (**a**: Fe/Na = 24; **b**: Fe/Mn = 40; **c**: Fe/Al = 40) and XRD patterns comparison of
561 wet (red line) and dry (black line) Ox-GR (**d**: Fe/Na = 24; **e**: Fe/Mn = 40; **f**: Fe/Al = 40). Noted that
562 these XRD patterns were collected at the similar operation conditions, so their intensities were
563 comparable.

564 **Fig. 2.** The XRD patterns in the 2θ range of 5° – 75° (**a**), 7° – 13° (**b**), 32° – 38° (**c**), and 60° – 65° (**d**)
565 and FTIR spectra (**e**: Mn system; **f**: Al system) of the dried Mn- or Al-incorporated Ox-GR samples.

566 **Fig. 3.** The transmission electron microscope and selected-area electron diffraction images of GR (**a**)
567 and Ox-GR samples (**b**: Fe/Na = 24; **c**: Fe/Mn = 40; **d**: Fe/Mn = 19; **e**: Fe/Al = 40; **f**: Fe/Al = 6.3);
568 high-resolution transmission electron microscope images of c-axis direction of Ox-GR (**g**: Fe/Na =
569 24; **h**: Fe/Mn = 19).

570 **Fig. 4.** The LCF fits of Mn K-edge XANES spectra (the circles are the experimental data, the lines
571 are the best-fit data, and the bottom lines are the difference plots) (**a**) and the obtained atomic
572 percentages of Mn(II), Mn(III), and Mn(IV) of Mn-incorporated Ox-GR (**b**).

573 **Fig. 5.** Release kinetics of cations and sulfate (**a**: Fe/Mn = 40; **b**: Fe/Al = 40), and release proportion
574 of cations and sulfate with the fraction of dissolved Fe for the final dried Ox-GR samples (**c**: Fe/Mn
575 = 40; **d**: Fe/Al = 40) dissolved in 2 M HCl solution.

576 **Fig. 6.** The As(III) adsorption kinetics on Ox-GR samples at pH 5 (**a**) and pseudo second-order kinetic
577 equation fitting normalized to mineral mass (**b**, $\frac{t}{q_t} = \frac{1}{k_2 q_e^2} + \frac{t}{q_e}$), and the dissolved SO₄²⁻ (**c**) and Mn
578 and Al (**d**) during kinetics; the ratios of As(V)/total As in the suspension (including solution and solid)
579 after As(III) adsorption for 8 h(**e**).

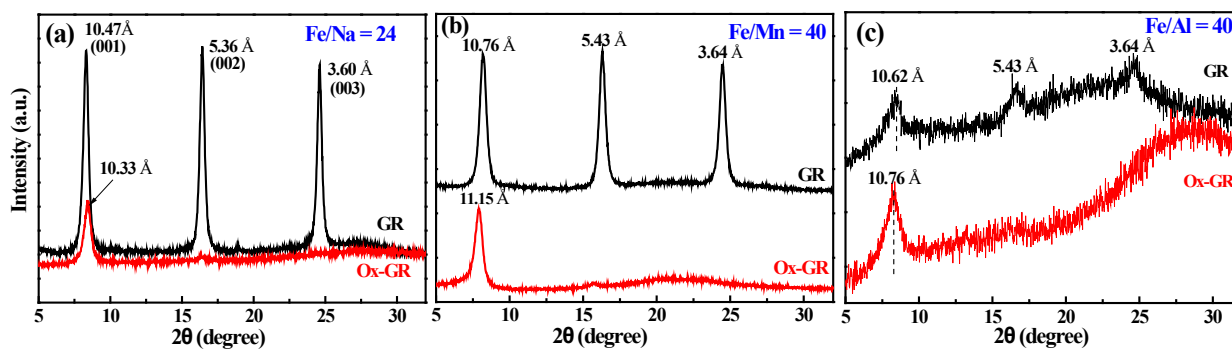
580 [Fig. 7](#). As K-edge EXAFS spectroscopy for the data (blank square) and shell-by-shell model fits (red
581 lines) for As(III) sorption kinetic samples (uncorrected for phase shifts): k^3 -weighted $\chi(k)$ spectra ([a](#))
582 and Fourier transform magnitude ([b](#)), and the fitted parameters are summarized in [Table S3](#).

583 [Fig. 8](#). Fitting results of O_{1s} and Mn_{2p} XPS of the Ox-GR sample with $Fe/Mn = 26$ before ([a and c](#))
584 and after ([b and d](#)) As(III) adsorption at pH 5.

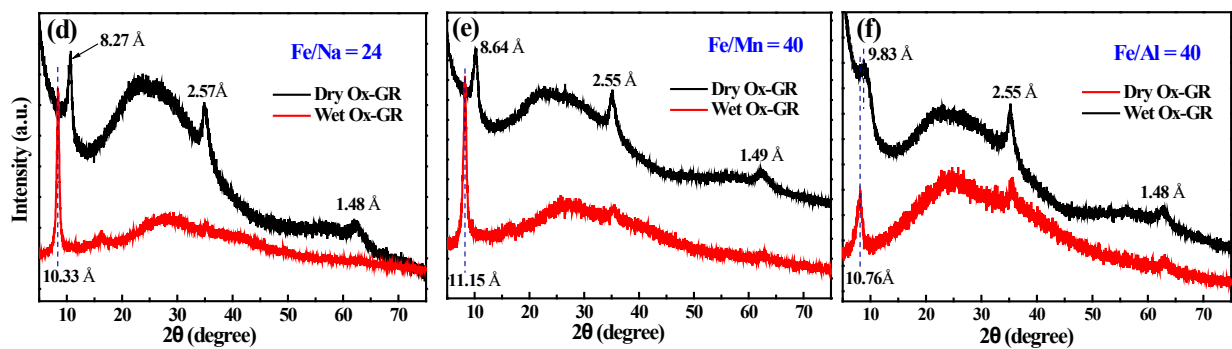
585

586

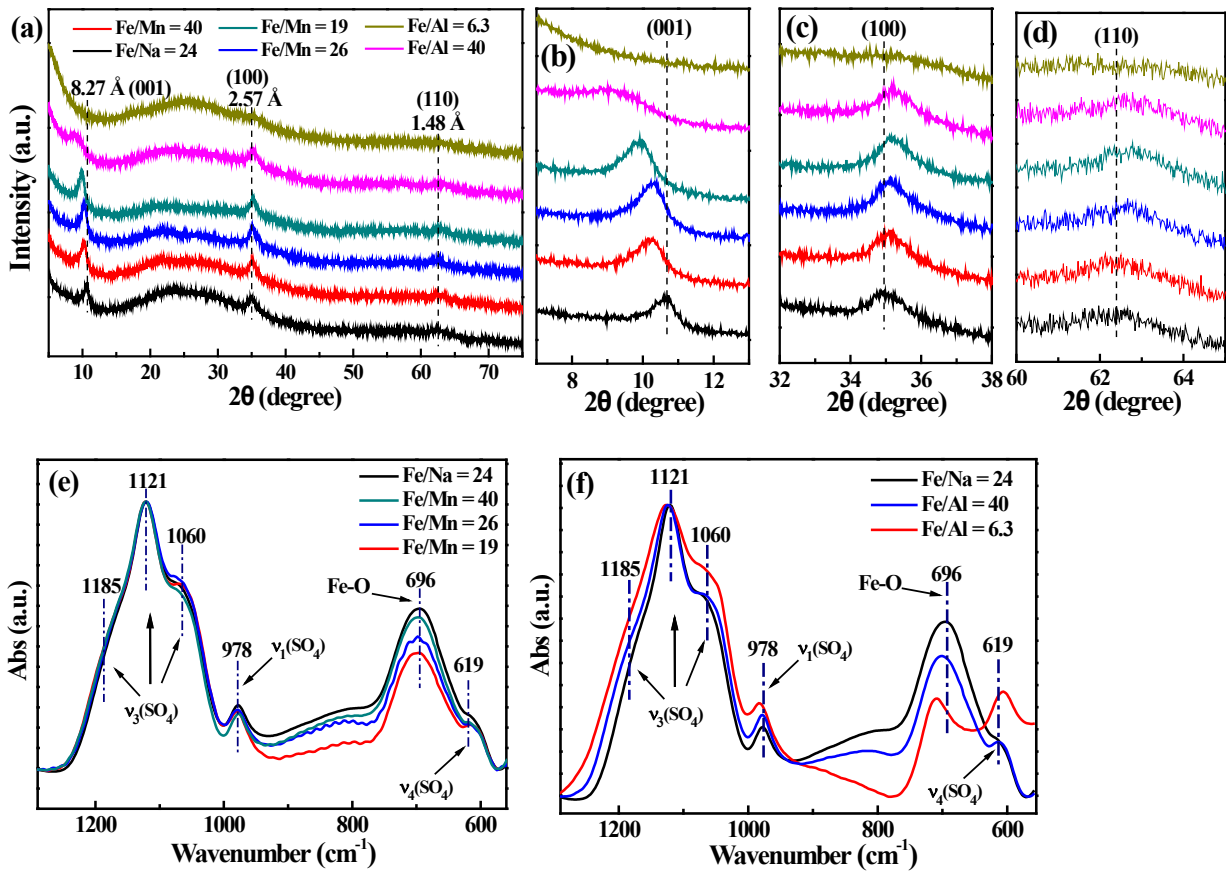
587



588



589 **Fig. 1.** XRD patterns of GR (black line) and its oxidation product of Ox-GR (red line) after adding
 590 H_2O_2 for ~ 40 min (a: Fe/Na = 24; b: Fe/Mn = 40; c: Fe/Al = 40) and XRD patterns comparison of
 591 wet (red line) and dry (black line) Ox-GR (d: Fe/Na = 24; e: Fe/Mn = 40; f: Fe/Al = 40). Noted that
 592 these XRD patterns were collected at the similar operation conditions, so their intensities were
 593 comparable.

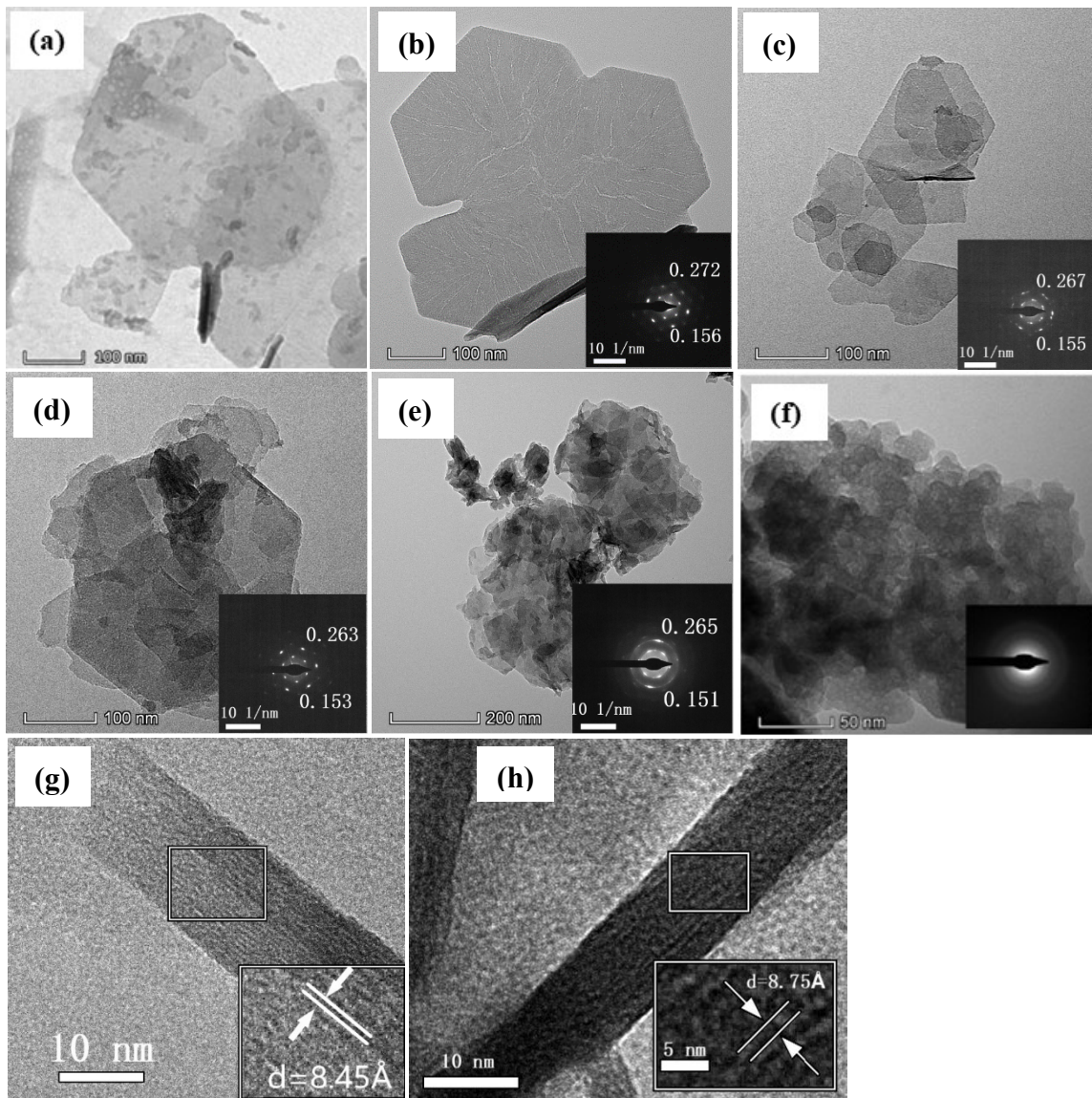


594

595

596 Fig. 2. The XRD patterns in the 2θ range of $5^\circ - 75^\circ$ (a), $7^\circ - 13^\circ$ (b), $32^\circ - 38^\circ$ (c), and $60^\circ - 65^\circ$ (d)

597 and FTIR spectra (e: Mn system; f: Al system) of the dried Mn- or Al-incorporated Ox-GR samples.



598

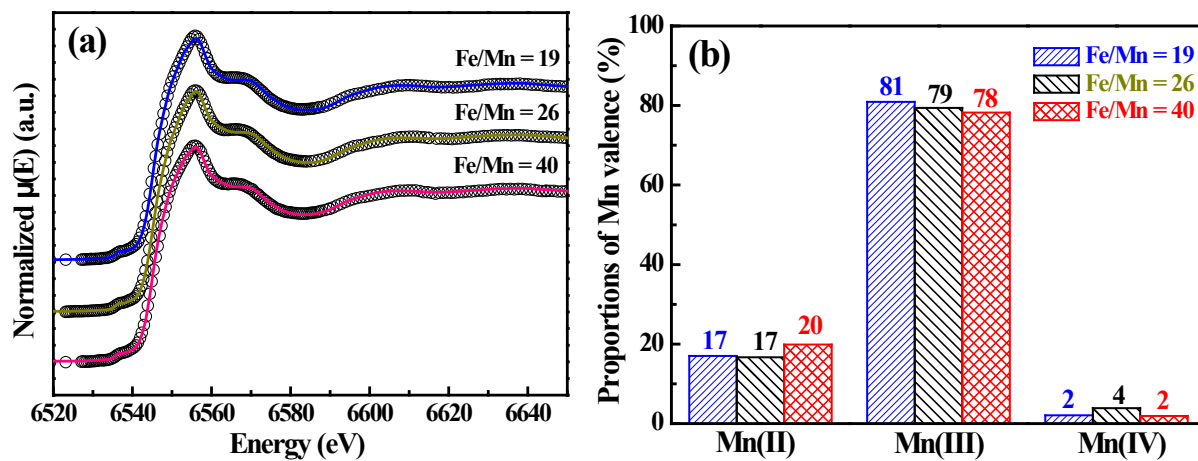
599

600

601

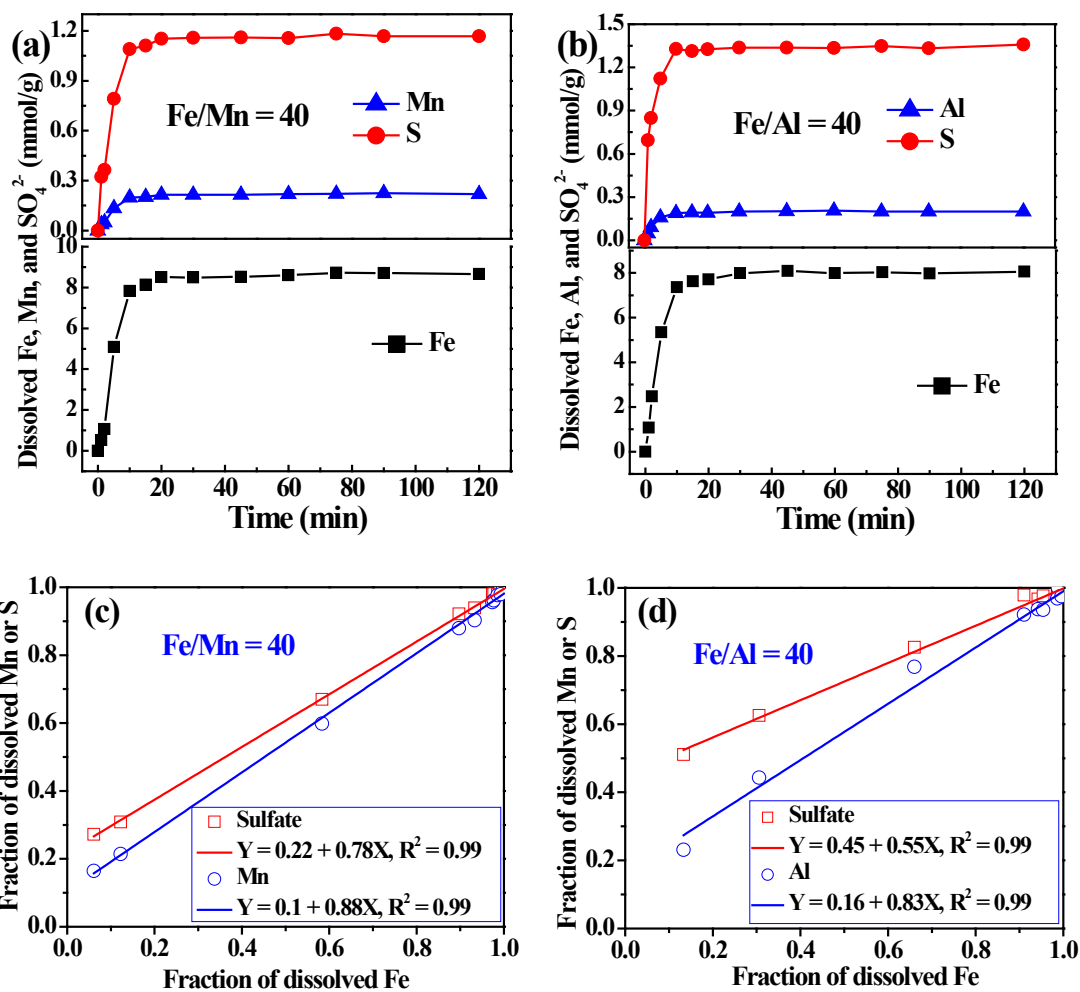
602

Fig. 3. The transmission electron microscope and selected-area electron diffraction images of GR (a) and Ox-GR samples (b: Fe/Na = 24; c: Fe/Mn = 40; d: Fe/Mn = 19; e: Fe/Al = 40; f: Fe/Al = 6.3); high-resolution transmission electron microscope images of c-axis direction of Ox-GR (g: Fe/Na = 24; h: Fe/Mn = 19).



603

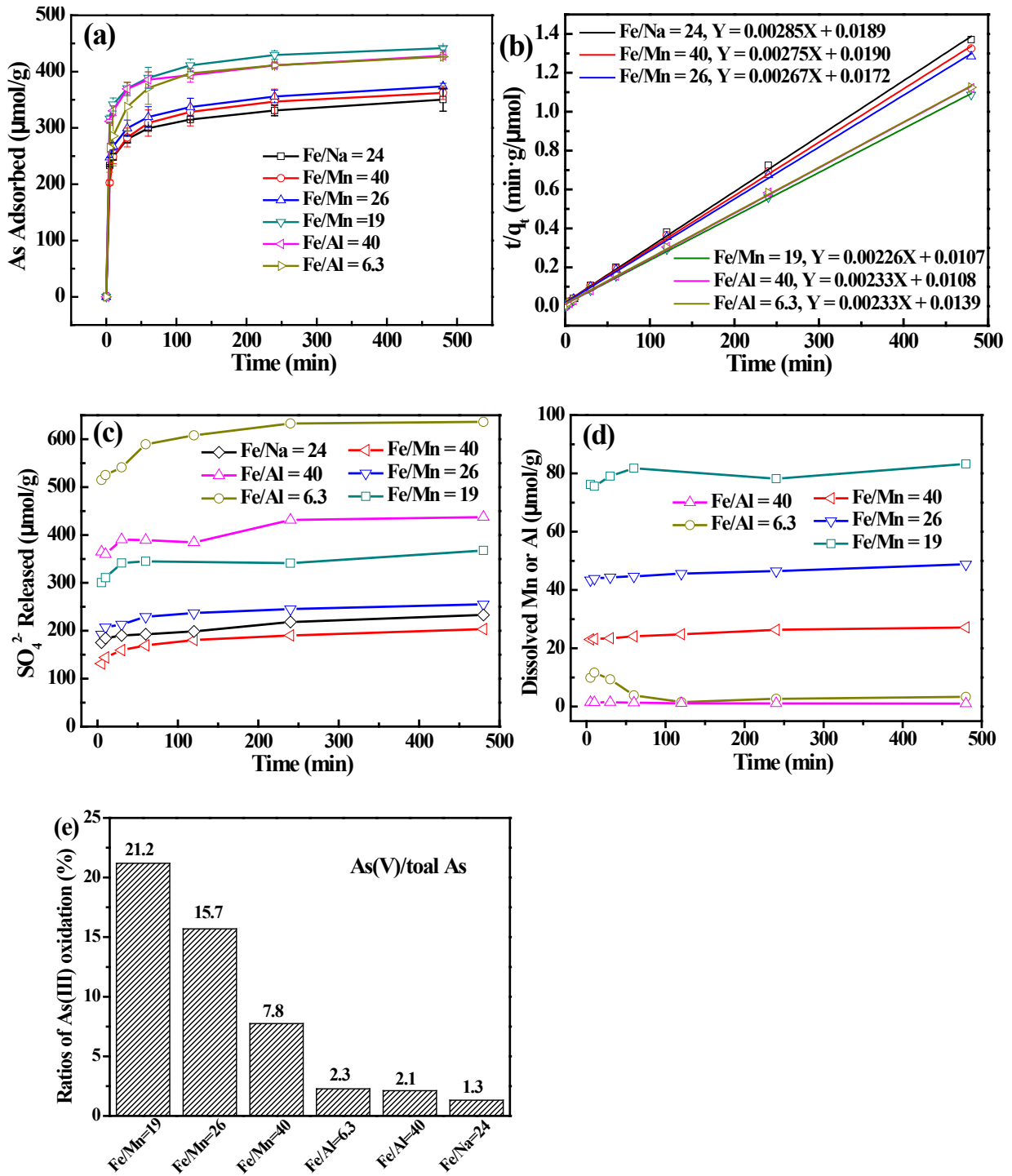
604 Fig. 4. The LCF fits of Mn K-edge XANES spectra (the circles are the experimental data, the lines
 605 are the best-fit data, and the bottom lines are the difference plots) (a) and the obtained atomic
 606 percentages of Mn(II), Mn(III), and Mn(IV) of Mn-incorporated Ox-GR (b).



607

608

609 **Fig. 5.** Release kinetics of cations and sulfate (a: Fe/Mn = 40; b: Fe/Al = 40), and release proportion
 610 of cations and sulfate with the fraction of dissolved Fe for the final dried Ox-GR samples (c: Fe/Mn
 611 = 40; d: Fe/Al = 40) dissolved in 2 M HCl solution.

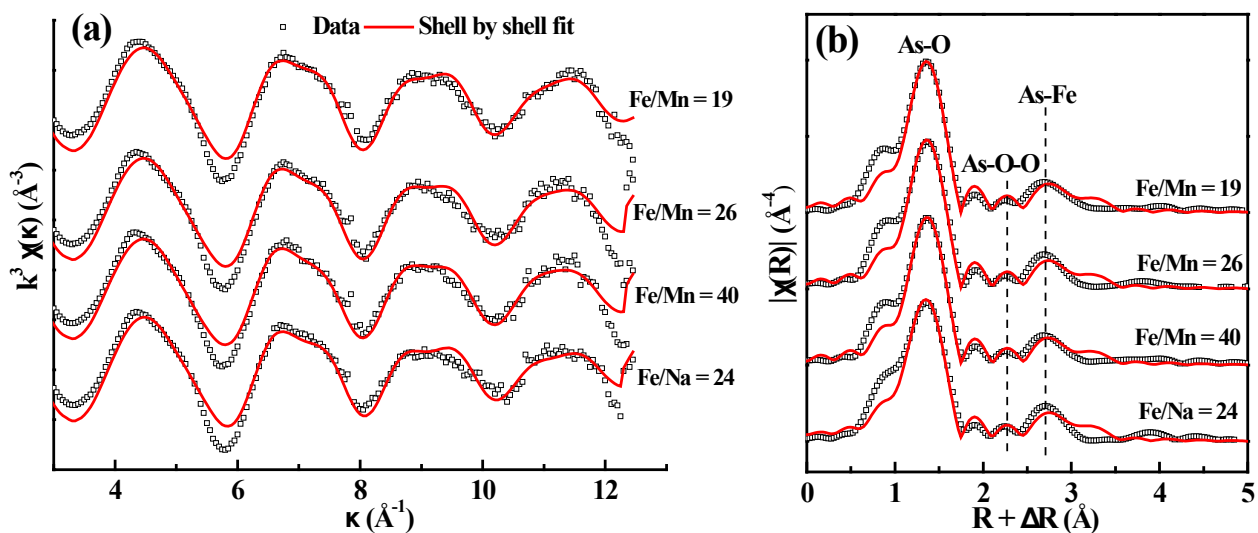


612

613

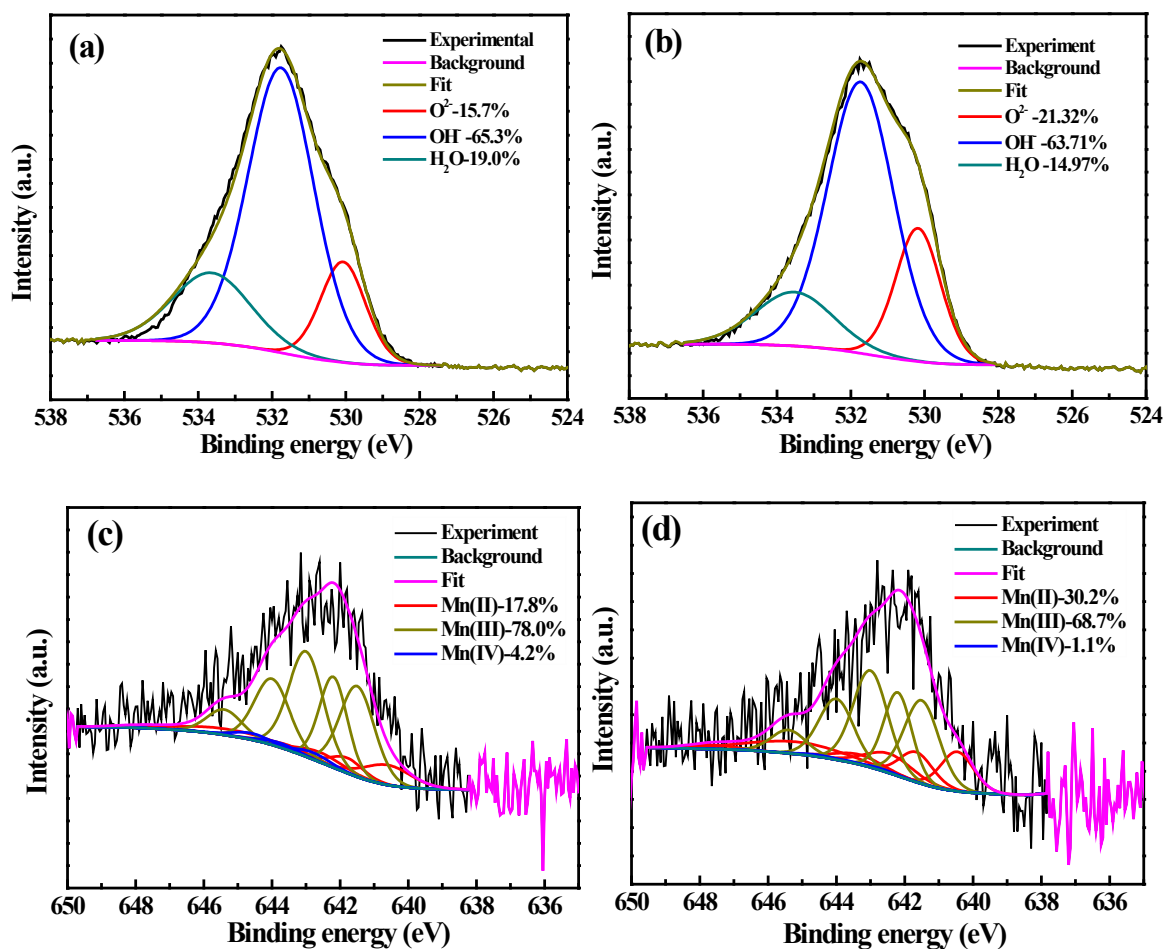
614

615 **Fig. 6.** The As(III) adsorption kinetics on Ox-GR samples at pH 5 (a) and pseudo second-order kinetic
 616 equation fitting normalized to mineral mass (b, $\frac{t}{q_t} = \frac{1}{k_2 q_e^2} + \frac{t}{q_e}$), and the dissolved SO_4^{2-} (c) and Mn
 617 and Al (d) during kinetics; the ratios of As(V)/total As in the suspension (including solution and solid)
 618 after As(III) adsorption for 8 h(e).



619

620 **Fig. 7.** As K-edge EXAFS spectroscopy for the data (blank square) and shell-by-shell model fits (red
 621 lines) for As(III) sorption kinetic samples (uncorrected for phase shifts): k^3 -weighted $\chi(k)$ spectra (a)
 622 and Fourier transform magnitude (b), and the fitted parameters are summarized in [Table 2](#).



623

624

625 **Fig. 8.** Fitting results of O_{1s} and Mn_{2p} XPS of the Ox-GR sample with Fe/Mn = 26 before (a and c)
 626 and after (b and d) As(III) adsorption at pH 5.

627